Dalton Transactions

PAPER

View Article Online
View Journal | View Issue

Facile template free synthesis of $KLa(MoO_4)_2$: Eu^{3+},Tb^{3+} microspheres and their multicolor tunable luminescence

Cite this: *Dalton Trans.*, 2014, **43**, 5382

Li Hou,[a] Shaobo Cui,[a] Zuoling Fu,*[a] Zhijian Wu,[b] Xihong Fu[c] and Jung Hyun Jeong*[d]

Received 7th November 2013,
Accepted 2nd January 2014

DOI: 10.1039/c3dt53151a

www.rsc.org/dalton

Trivalent rare-earth (RE^{3+} = Eu^{3+}, Tb^{3+}) ion activated $KLa(MoO_4)_2$ microspheres have been synthesized at 180 °C *via* a facile hydrothermal route without using any templates, surfactant, or other organic additives. X-ray diffraction (XRD), field emission-scanning electron microscopy (FE-SEM), photoluminescence (PL), and photoluminescent excitation spectra (PLE) were employed to characterize the samples. It is found that the pH value in the initial solution is responsible for crystal phase, shape determination and emission intensity of final products. The possible formation mechanism for products with uniform spheres has been presented. Furthermore, a systematic study on the photoluminescence of RE^{3+} (RE^{3+} = Eu^{3+}, Tb^{3+}) doped $KLa(MoO_4)_2$ samples has been explored in order to obtain the multicolor tunable emission by varying the Tb^{3+}/Eu^{3+} ratio. The tunable luminescence may be potentially applied in fields such as solid state lighting and field emission displays.

1. Introduction

In recent years, there has been a growing interest in the generation of white light sources for a range of applications, such as solid-state lighting, multicolor three-dimensional displays, back lights, fluorescent sensors, and so on.[1–7] In the field of solid-state lighting, white light emitting diodes (W-LEDs), as a new generation of light sources, have many advantages such as low power consumption, environmental protection, long serving lifetime, and high luminous efficiency.[8–15] Generally, W-LEDs can be fabricated by combining GaN-based blue chips with YAG:Ce^{3+} yellow phosphors, but lacks a red component, resulting in a low color rendering index (CRI).[16] So another way of obtaining white LEDs is sought out, utilizing a near-UV LED chip combined with phosphors, including red, green and blue emitting phosphors, designed to convert the UV light to visible light.[17] In order to obtain a higher efficiency white LED with an appropriate color temperature and a higher color-rendering index, a new approach using near-ultraviolet (nUV) InGaN-based LED chip coated with blue/green/red tricolor phosphors was introduced.[18] However, the lack of effective red phosphor blocks the development of white LEDs because few red phosphors can be excited efficiently by blue or nUV light. Therefore, it is of high interest to search for a stable red-emitting phosphor and white light emission in single host with a high absorption in the near-ultraviolet or blue spectral region.[19–24]

Recently, micro/nanocrystals doped with rare-earth ions have played an important role in modern lighting and display fields due to their unique electronic, optical, and chemical properties.[25,26] Compared with conventional luminescent materials,[27,28] such as organic fluorescent dyes and semiconductor quantum dots, rare-earth ion-doped materials have low photobleaching, narrow emission bands, and longer luminescent lifetimes.[29–32] As a fascinating group of inorganic-functional materials, molybdates have attracted special attention because of their wide use as catalysts, luminescent materials, inhibitive pigments, and so on,[33–35] especially double alkaline rare-earth molybdates $ARE(MoO_4)_2$ (A = Na, K; RE = trivalent rare-earth cation), which share the scheelite-like ($CaWO_4$) isostructure with the tetragonal space group $I4_1/a$, in which Mo^{6+} is coordinated by four oxygen atoms in a tetrahedral site and the rare-earth ions or alkali metal ions are eight coordinated.[36] The concentration quenching effect hardly occurs in ARE $(MoO_4)_2$ (A = Na; RE = Y, Eu) doped with RE ions. Therefore, further exploration of well-controlled shapes and size of ARE $(MoO_4)_2$ is still an important research subject.

However, rare-earth doped $KLa(MoO_4)_2$ has been reported in previous work.[37–39] In this paper, we study the synthesis of

[a]*State Key Laboratory of Superhard Materials, College of Physics, Jilin University, Changchun 130012, China. E-mail: zlfu@jlu.edu.cn; Fax: +86-431-85167966; Tel: +86-431-85167966*
[b]*State Key Laboratory of Rare Earth Resources Utilization, Changchun Institute of Applied Chemistry, Chinese Academy of Sciences, Changchun 130022, China*
[c]*Changchun Institute of Optics, Fine Mechanics and Physics, Chinese Academy of Sciences, Changchun 130033, China*
[d]*Department of Physics, Pukyong National University, Busan 608-737, South Korea. E-mail: jhjeong@pknu.ac.kr; Fax: +82-51-6295549; Tel: +82-51-6295564*

rare-earth molybdates $KLa(MoO_4)_2$:Eu^{3+}/Tb^{3+} microspheres *via* the hydrothermal process without any organic solvents or surfactants. The hydrothermal synthesis method is one of the most important "soft chemistry" techniques for the synthesis of phosphor materials with higher uniformity in particle size distribution and non-agglomeration.[40,41] Moreover, the luminescence intensity can be enhanced in the uniform microspheres over that of agglomerates of distorted particles.[42,43] The effects of the pH value in the initial solution on crystal phase, morphology and photoluminescence of final products were studied, and a possible formation mechanism for the microspheres was proposed. Finally, the luminescence properties of Eu^{3+}/Tb^{3+}-doped sphere-like $KLa(MoO_4)_2$ phosphors were investigated in detail and the energy transfer mechanism between rare-earth ions was discussed.

2. Experimental details

2.1. Preparation of Eu^{3+}/Tb^{3+}-doped $KLa(MoO_4)_2$ microcrystals

2.1.1. Materials. Lanthanum oxide, terbium oxide and europium oxide (all 99.99%) were used as the starting raw materials. All other chemicals used were analytical grade. $La(NO_3)_3$, $Tb(NO_3)_3$ and $Eu(NO_3)_3$ solutions were prepared by dissolving La_2O_3, Tb_2O_3 and Eu_2O_3 in dilute HNO_3 under stirring and heating, until the powders were all dissolved. The ammonium molybdate tetrahydrate ($(NH_4)_6Mo_7O_{24}\cdot4H_2O$) was used as the molybdenum source and potassium hydroxide (KOH) as the potassium source. For the hydrothermal treatment, we used 60 mL Teflon cups.

2.1.2. Synthesis. Appropriate amounts of solutions of $La(NO_3)$ and $Eu(NO_3)$ were mixed together with strong magnetic stirring at room temperature for 10 minutes. Next the stoichiometric amounts of $(NH_4)_6Mo_7O_{24}\cdot4H_2O$ were dissolved in 20 ml distilled water with strong magnetic stirring at room temperature for 10 minutes to form an aqueous solution. Next, the same solutions were adjusted to pH = 4, 5, 6, 7, 8 or 9 by adding dropwise into the above solutions a desired amount of KOH (5 M) under vigorous stirring before hydrothermal treatment. KOH immediately reacted with the molybdenum source and rare-earth nitrate solutions, and a slurry-like white precipitate was formed. The mixture was stirred again for 1 h. Finally, the mixture was introduced into a Teflon bottle held in a stainless steel autoclave, sealed, and maintained at 180 °C for 12 h. After natural cooling, the hydrothermal product was collected *via* centrifugation, washed with distilled water and ethanol, and then dried in air at 60 °C for 8 h. Finally, the uniform distribution spherical $KLa_{(1-x)}(MoO_4)_2$:xEu^{3+} microcrystals were obtained. The experiment was repeated under similar conditions for the synthesis of $KLa_{(1-x-y)}(MoO_4)_2$:xEu^{3+}, yTb^{3+}. To investigate the intermediates of the spherical $KLa(MoO_4)_2$:Eu^{3+}, the synthesis was stopped at different stages during the synthesis process.

2.2. Characterization

X-ray powder diffraction (XRD) measurements were performed on a Rigaku-Dmax 2500 diffractometer at a scanning rate of 15° min^{-1} in the 2θ range from 10 to 65°, with graphite monochromatized Cu Kα radiation (λ = 0.15405 nm). The morphology and size of the obtained samples were examined by a field emission-scanning electron microscope (FE-SEM, XL30, Philips). The ultraviolet-visible photoluminescence (PL) excitation and emission spectra were recorded with a Hitachi F-7000 spectrophotometer equipped with a Xe-lamp as an excitation source. The luminescent dynamics were investigated using a three part laser system consisting of a (i) Nd:YAG pumping laser (1064 nm), (ii) third-order harmonic generator (blue laser at 486 nm), and (iii) tunable optical parametric oscillator (OPO, Continuum Precision II 8000); with a pulse duration of 10 ns, repetition frequency of 10 Hz, and line width of 4–7 cm^{-1}. All the measurements were performed at room temperature.

3. Results and discussion

3.1. Phase identification and morphology of the $KLa(MoO_4)_2$:Eu^{3+} microcrystals

The composition and phase purity of the as-prepared powder samples were first examined by XRD. Fig. 1 shows the XRD patterns of the hydrothermal reaction products obtained at different pH values for 12 h at 180 °C. The most suitable pH value for the synthesis of single phase crystalline $KLa(MoO_4)_2$:Eu^{3+} powders was investigated by varying the base (KOH) concentration used in the reaction system. When the value of pH ≤ 5 (Fig. 1(a) pH = 4 and (b) pH = 5), impurity peaks were detected in the XRD patterns, whereas beginning with pH = 6 (Fig. 1(c)), all of the peaks were consistent with the literature data (JCPDS no. 40-0466). The crystallization reached completion without impurity phase at the pH value of 7 (Fig. 1(d)),

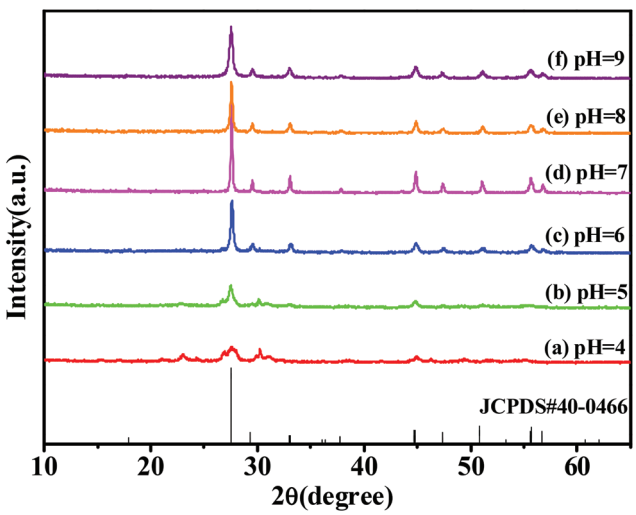

Fig. 1 XRD patterns of the $KLa(MoO_4)_2$:Eu^{3+} at different pH values (a) pH = 4; (b) pH = 5; (c) pH = 6; (d) pH = 7; (e) pH = 8; (f) pH = 9.

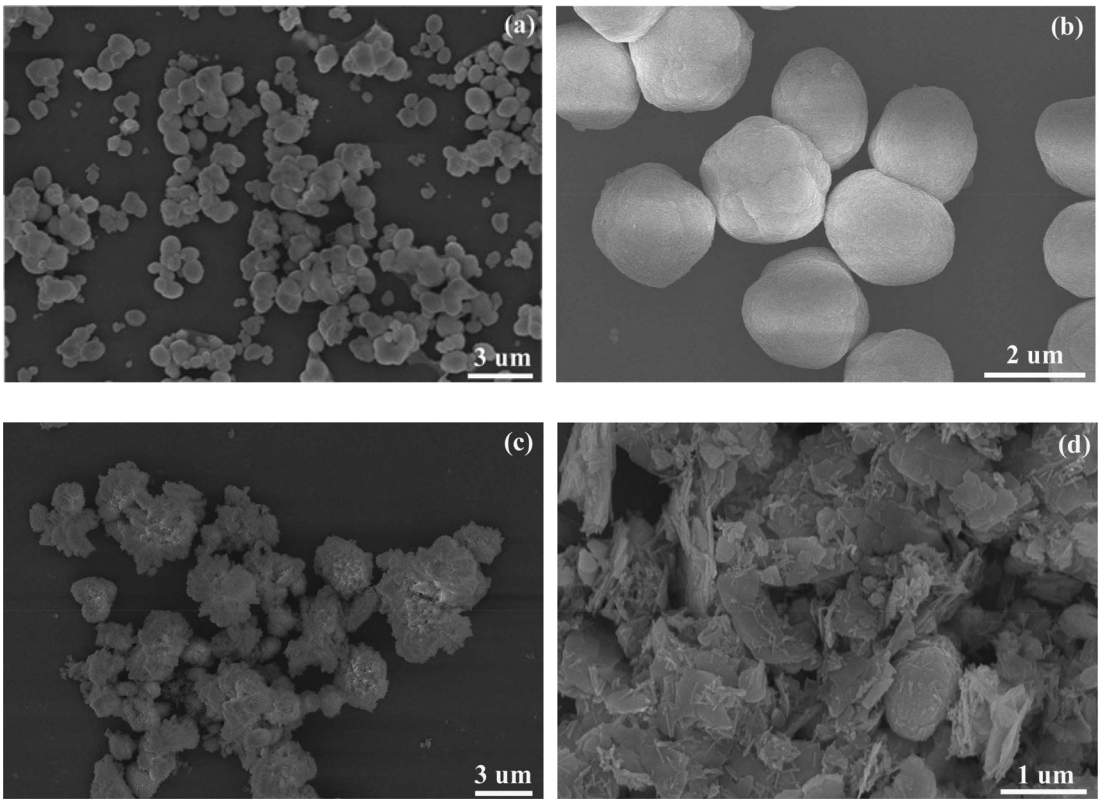

Fig. 2 FE-SEM images of $KLa(MoO_4)_2:Eu^{3+}$ crystallites prepared hydrothermally at 180 °C for 12 h at (a) pH = 6; (b) pH = 7; (c) pH = 8; (d) pH = 9.

indicating that the Eu^{3+} ions were completely dissolved in the $KLa(MoO_4)_2$ host lattice at the current doping concentration without inducing significant changes in the crystal structure. In addition, when the pH value varied from 8 to 9, we also obtained the pure phase (Fig. 1(e) pH = 8 and (f) pH = 9). The above-stated results indicate that the pH value is very important for preparing the pure phase $KLa(MoO_4)_2$, which is in good accordance with the observed FE-SEM images shown in Fig. 2.

The morphology and size of phosphors are important for their application in coatings on lighting devices. To fully understand the effect of pH value on the microstructure and morphology of the synthesized samples, controlled experiments were conducted to find the optimal morphology. Fig. 2 shows the morphology evolution of resultant $KLa(MoO_4)_2:Eu^{3+}$ crystallites from different starting pH values after hydrothermal treatment at 180 °C for 12 h. When pH = 6 (Fig. 2(a)), the product exhibited irregular spheres consisting of agglomerated particles with an average size around 1 μm. When the pH value was 7, $KLa(MoO_4)_2:Eu^{3+}$ microcrystals retain monodisperse, non-aggregated and smooth microspheres with an average diameter of about 2 μm (Fig. 2(b)). As the pH value of the reaction system was enhanced to 8 (Fig. 2(c)), the product exhibited some dissolved spheres. The morphology changed again when the pH value of the solution was increased to 9, the product exhibited some microplates with many nanowires (Fig. 2(d)).

On the basis of the experimental results, the pH value of the precursor was found to be an important factor influencing pure-phase formation and uniform morphology of the final product in the hydrothermal procedure.[44–46] KOH was critical for directing the intrinsic shapes of the crystals due to its characteristic symmetry and structure,[47] and would change the growth rate of crystallographic planes with different surface energies so as to form different crystallite morphologies.[44,48–52] Therefore, a crystallization pH value of 7 was optimal.

3.2. Growth mechanism for the spherical $KLa(MoO_4)_2:Eu^{3+}$ microcrystals

Crystal growth mechanisms in solution are so complicated that the actual crystallization mechanism remains an open question. Considering that there are no additional templates and surfactants in the present case, it is reasonable that the growth and formation of microstructure is neither catalyst-assisted nor template-assisted since the only source materials used in this case are pure $(NH_4)_6Mo_7O_{24}{\cdot}4H_2O$, $Eu(NO_3)_3$ and KOH. The growth process of $KLa(MoO_4)_2:Eu^{3+}$ microcrystals was explored by observing the morphological evolution of samples over the reaction time (Fig. 3). Before the hydrothermal reaction, tiny microsheets containing nanoparticles (Fig. 3(a)) were formed after the pH value of the solution was adjusted. Once the $KLa(MoO_4)_2$ nuclei were formed, new reactants were continuously arriving at the site. Fig. 3(b) shows the morphology of the products synthesized after the precipitate

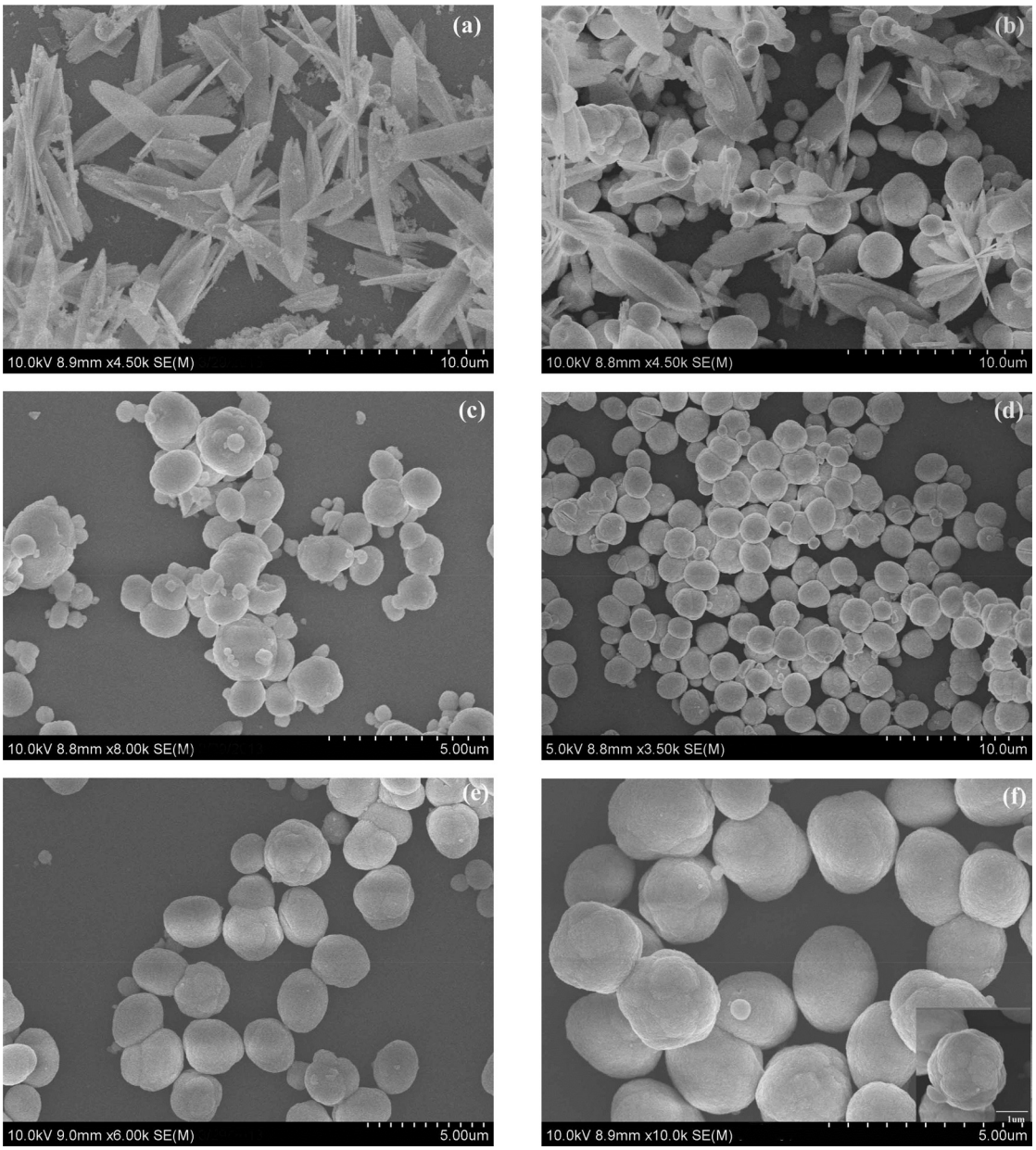

Fig. 3 FE-SEM images of the products synthesized at 180 °C and pH = 7 with different hydrothermal reaction times: (a) just after the pH value of the solution was adjusted; (b) after stirring for 1 h before hydrothermal treatment; after hydrothermal treatment for (c) 0.5 h, (d) 3 h, (e) 7 h and (f) 12 h.

was stirred for 1 h. We obtained self-assembled microflowers with intercrossing petals, including some microspheres, demonstrating that the crystalline nanoparticles tend to aggregate due to their higher surface energy and Ostwald's ripening process driven by the minimization of interfacial energy by reducing the nucleating centers.[53] After hydrothermal treatment for 0.5 h, the self-assembled microflowers disappeared completely, irregular spherical-like nucleation acted as centers of crystallization, and crystal growth then followed, where bigger particles grew at the expense of small crystals, as shown in Fig. 3(c). As the reaction proceeded, the crystals with rough surface were further grown on the basis of the framework of a sphere (Fig. 3(d)). Upon continuing the reaction, the surface of the spherical-like microcrystals became smooth (Fig. 3(e)). Finally, perfect spherical $KLa(MoO_4)_2$:Eu^{3+} microcrystals were obtained (Fig. 3(f)). From the thermodynamic viewpoint, it is believed that the reduction in surface energy is the primary driving force for simple particle growth, the further reduction in surface energy due to the minimization of high surface energy faces will drive the morphology evolution. From the above analysis, it may be that the spherical-like microcrystals were formed under mild hydrothermal conditions through a homogeneous nucleation, crystallization, aggregation and oriented self-assembling process. The process

Scheme 1 Schematic illustration of the formation and morphology evolution of $KLa(MoO_4)_2:Eu^{3+}$ microcrystals in the whole synthetic process.

of the morphology evolution of spherical $KLa(MoO_4)_2:Eu^{3+}$ microcrystals is schematically illustrated in Scheme 1.

3.3. Optical properties

3.3.1. Luminescent properties of $KLa(MoO_4)_2:Eu^{3+}$ microspheres. The Eu^{3+} ion is a well-known red-emitting activator in commercial phosphors because the emission of the rare-earth Eu^{3+} ion consists usually of lines in the red spectral area due to the $^5D_0$–^7F_J (J = 1, 2, 3, 4, 5 and 6) transitions. Fig. 4 shows the PL excitation and emission spectra of $KLa_{0.96}(MoO_4)_2:0.04Eu^{3+}$ phosphors. The excitation spectrum (Fig. 4, left) was obtained by monitoring the emission of the Eu^{3+} $^5D_0$–$^7F_2$ transition at 616 nm. It can be observed clearly that the excitation spectrum exhibits a broad excitation band centered at 275 nm, which is ascribed to the O–Mo charge-transfer transition (ligand to metal charge transfer (LMCT)).[54,55] In the longer wavelength region (360–500 nm), Eu^{3+} doped phosphors usually have effective and intrinsic absorption due to the intraconfigurational 4f–4f transition of Eu^{3+} at about 395 nm ($^7F_0$–$^5L_6$) and 465 nm ($^7F_0$–$^5D_2$), which makes it match well with the near-UV and blue GaN-based LED chips as an efficient red light emitting phosphor. The emission spectrum (Fig. 4, right) was obtained under 275 nm excitation and displays the characteristic emission peaks of the Eu^{3+} ions with a strong emission at 616 nm, and the sample displays a bright red color to the naked eye (inset in Fig. 4).

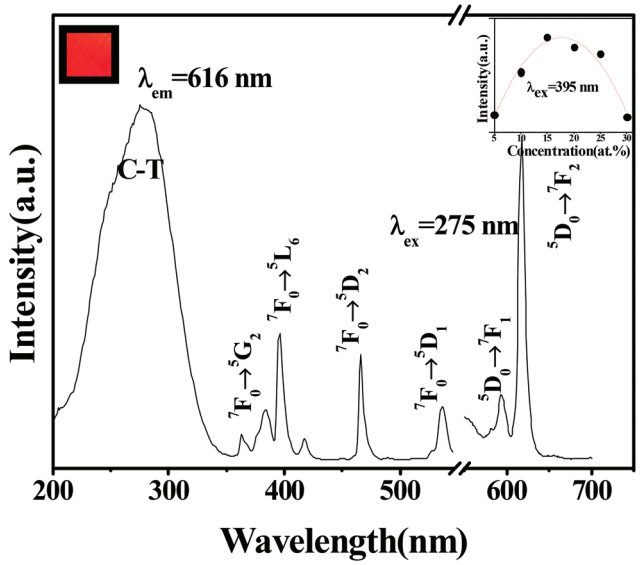

Fig. 4 PL excitation (left) and emission (right) spectra of $KLa(MoO_4)_2:0.04Eu^{3+}$ microcrystals.

The emission peaks of Eu^{3+} are assigned to transitions from the excited $^5D_0$ state to ^7F_J (J = 1, 2) levels. It is well known that the f–f transitions of the trivalent lanthanides are little affected by the crystal field, but a few are sensitive to the chemical environment. Generally, if Eu^{3+} ions are embedded in a site with inversion symmetry, the $^5D_0$–$^7F_1$ magnetic dipole transition is domination, while in a site without inversion symmetry, the $^5D_0$–$^7F_2$ electric dipole transition is the strongest. In the $KLa(MoO_4)_2:Eu^{3+}$ system, we can use the $I(^5D_0$–$^7F_2)/I(^5D_0$–$^7F_1)$ emission intensity ratio as a measure of the site symmetry of Eu^{3+}. When the pH = 7, the intensity of the red $^5D_0$–$^7F_2$ transition of Eu^{3+} at 616 nm is about five times stronger than that of $^5D_0$–$^7F_1$, which significantly indicates that the Eu^{3+} ions occupy a center of asymmetry in the crystal lattice.[56,57] The transition $^5D_0$–$^7F_2$ is much stronger than the transition $^5D_0$–$^7F_1$, which is favorable to improve the color purity of the red phosphor. Besides, in these Eu-doped samples, it can be seen that the optimal concentration of Eu^{3+} is 15 at% (inset in Fig. 4).

With a concentration of 4 at% for Eu^{3+}, the $KLa(MoO_4)_2$ phosphors were prepared arising from different starting pH values (pH = 6, 7, 8, 9) and the evolution of the emission and excitation spectra are presented in Fig. 5. All spectra are similar in shape and location, excluding relative intensities. The excitation spectra were monitored at an emission wavelength of 616 nm for the $^5D_0$→$^7F_2$ transition. Upon UV excitation at 395 nm, the $KLa(MoO_4)_2:Eu^{3+}$ samples exhibit strong red luminescence. The emission spectra show the well-known $^5D_0$–^7F_J (J = 1, 2) emission lines of the Eu^{3+} ions with strong emission for J = 2 at 616 nm. With the change of pH value from 6 to 9, the excitation and emission intensities increase gradually and reach a maximum at pH = 7. Because the pH value is 7, the crystallinity is clearly improved and a high density of surface states exist in the luminescence "dead layer", which will reduce the rate of surface recombination.[58] To fully understand the effect of pH value on the luminescence, we also produced decay curves (Fig. 6) of $KLa(MoO_4)_2:0.04Eu^{3+}$ with different starting pH values (pH = 6, 7, 8, 9). From Fig. 6, it can be observed that the luminescence lifetime of Eu^{3+} ions for pH = 7 was about 0.594 ms. The lifetimes of Eu^{3+} ions were 0.555, 0.265 and 0.253 ms for pH = 6, 8 and 9, respectively. The lifetimes diminished obviously for pH values other than 7, which further confirmed that the differences in the surface recombination centers have an important effect on the luminescent intensity. Therefore, the luminescent intensity of the product at pH = 7 is the strongest due to the influence of the reduced surface recombination. Due to the similarity in spectral patterns, the emission spectra under 465 nm excitation were not displayed and discussed here. In summary, the uniform and well-crystallized $KLa(MoO_4)_2:Eu^{3+}$ microspheres synthesized in our experiment can be used as a red component for white light emitting diodes (W-LEDs).

3.3.2. Multicolor tunable luminescence of $KLa(MoO_4)_2:Eu^{3+}/Tb^{3+}$ microspheres. It is well-known that the Tb^{3+} ion is frequently used as an activator of green emitting luminescent

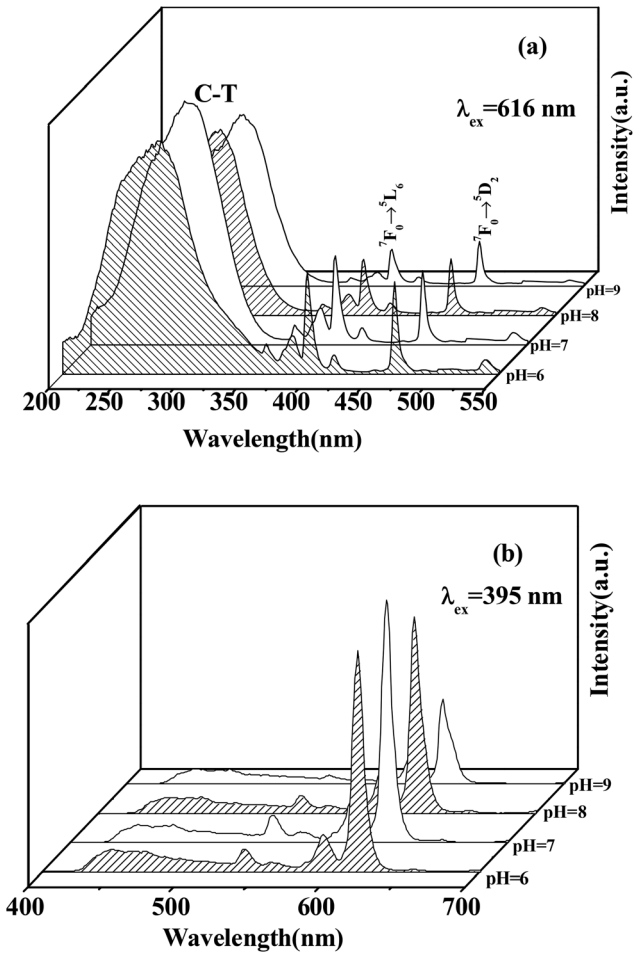

Fig. 5 PL excitation spectra (a) and PL emission spectra (b) of $KLa_{0.96}(MoO_4)_2$:0.04Eu^{3+} microcrystals prepared hydrothermally at 180 °C for 12 h from different starting pH values.

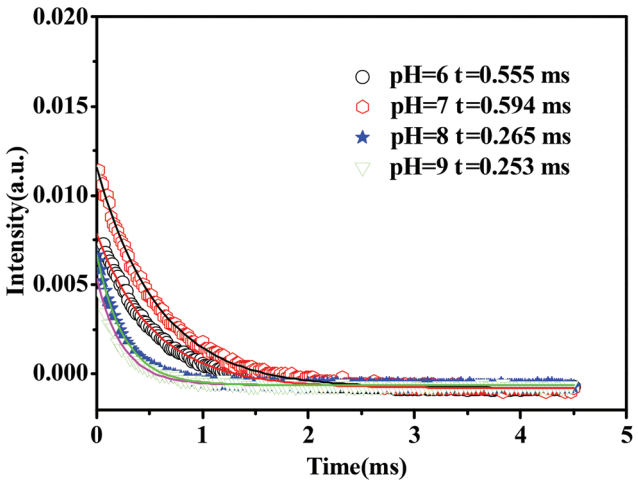

Fig. 6 Decay curves of the $KLa_{0.96}(MoO_4)_2$:0.04Eu^{3+} samples for different starting pH values (pH = 6, 7, 8, 9).

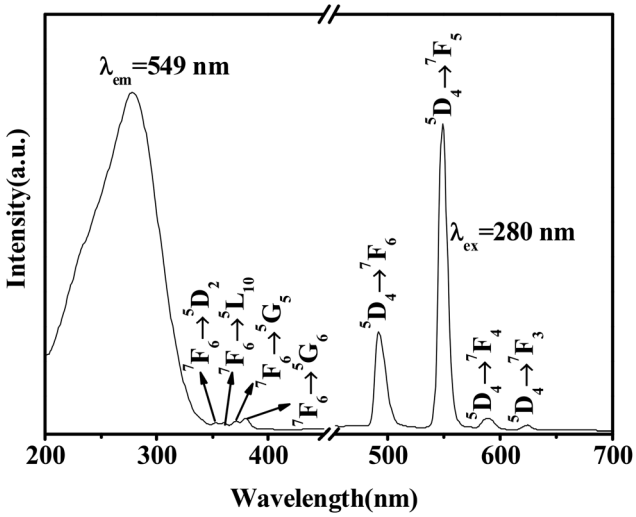

Fig. 7 PL excitation and emission spectra of $KLa(MoO_4)_2$:0.04Tb^{3+} microcrystals.

materials due to its predominant $^5D_4 \rightarrow {}^7F_5$ transition. Fig. 7 shows the PL excitation and emission spectra of $KLa_{0.96}(MoO_4)_2$:0.04Tb^{3+} phosphors. The excitation spectrum (Fig. 7, left) was obtained by monitoring the emission of the Tb^{3+} $^5D_4 \rightarrow {}^7F_5$ transition at 549 nm. It can be observed clearly that the excitation spectrum exhibits the broad excitation band centered at 280 nm in the range of 200–300 nm, which is ascribed to the O–Mo charge-transfer (C-T) transition.[55,56] The characteristic f→f transition lines within the Tb^{3+} $4f^8$ configuration in the longer wavelength region were assigned as the transitions from the $^7F_6$ ground state to the different excited states of Tb^{3+}, that is, 353 nm ($^7F_6 \rightarrow {}^5D_2$), 360 nm ($^7F_6 \rightarrow {}^5L_{10}$), 371 nm ($^7F_6 \rightarrow {}^5G_5$) and 379 nm ($^7F_6 \rightarrow {}^5G_6$).[59] The obtained emission spectrum (Fig. 7, right) of the $KLa_{0.96}(MoO_4)_2$:0.04Tb^{3+} phosphors consists of f→f transition lines within $4f^8$ electron configuration of Tb^{3+}, that is, $^5D_4 \rightarrow {}^7F_6$ (489 nm) in the blue region and $^5D_4 \rightarrow {}^7F_5$ (549 nm) in the green region, as well as $^5D_4 \rightarrow {}^7F_4$ (589 nm) and $^5D_4 \rightarrow {}^7F_3$ (622 nm) in the red region. The strongest one is the green emission of Tb^{3+} located at 549 nm.

In order to realize the multicolor tunable luminescence, Tb^{3+}, Eu^{3+} ions co-doped $KLa(MoO_4)_2$ phosphors were also prepared in our work. Fig. 8 shows the PL emission spectrum of $KLa_{0.90}(MoO_4)_2$:0.04Tb^{3+},0.06Eu^{3+} phosphors. Under excitation at 380 nm, the red (616 nm, Eu^{3+}), green (549 nm, Tb^{3+}) and blue (489 nm, Tb^{3+}) emission bands can be excited concurrently besides O–Mo broad band transition about 450 nm. Therefore, we can speculate that there exists energy transfer among Tb^{3+} and Eu^{3+} ions as well as the O–Mo C-T transition. In addition, it can be also seen in Fig. 9 that there is overlap between the emission spectrum of Tb^{3+} and the excitation spectrum of Eu^{3+}, so energy transfer may exist in the $KLa(MoO_4)_2$:Tb^{3+},Eu^{3+} microspheres.[60–62] Besides, when monitoring with 486 nm laser light (Fig. 10), it can be observed that the emission spectrum (red line) simultaneously contains the

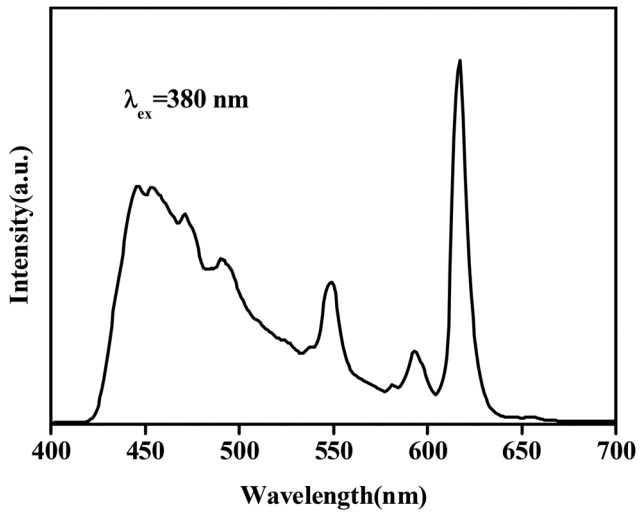

Fig. 8 PL emission spectrum of $KLa_{0.9}(MoO_4)_2$:$0.04Tb^{3+}$,$0.06Eu^{3+}$ microcrystals.

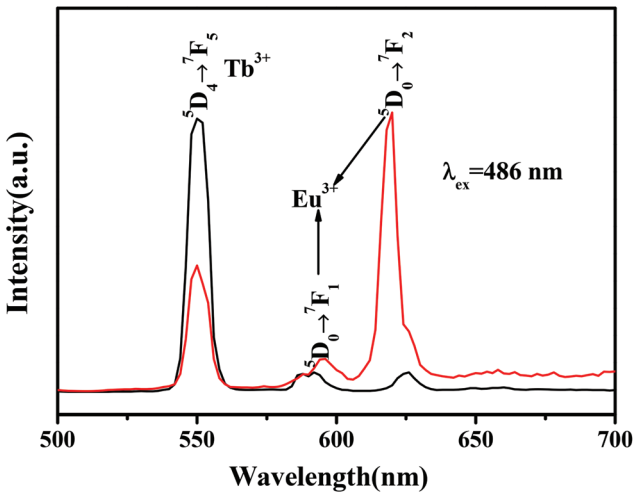

Fig. 10 Emission spectra of the $KLa_{0.96}(MoO_4)_2$:$0.04Tb^{3+}$ (black line) and $KLa_{0.84}(MoO_4)_2$:$0.04Tb^{3+}$,$0.12Eu^{3+}$ (red line) microcrystals.

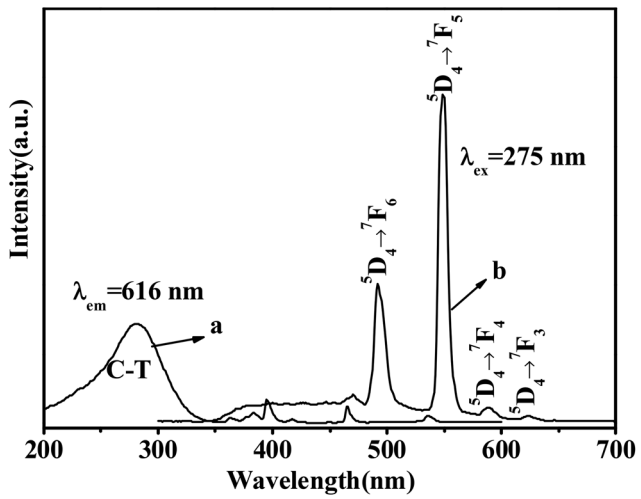

Fig. 9 Excitation spectrum (a) of the $KLa_{0.96}(MoO_4)_2$:$0.04Eu^{3+}$ and emission spectrum (b) of the $KLa_{0.96}(MoO_4)_2$:$0.04Tb^{3+}$ microcrystals.

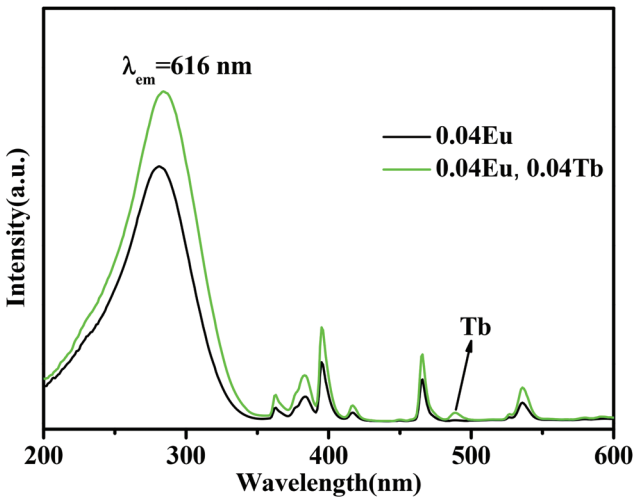

Fig. 11 Excitation spectra of the $KLa_{0.96}(MoO_4)_2$:$0.04Eu^{3+}$ and $KLa_{0.92}(MoO_4)_2$:$0.04Eu^{3+}$,$0.04Tb^{3+}$ microcrystals.

592 nm ($^5D_0$–$^7F_1$) and 616 nm ($^5D_0$–$^7F_2$) of Eu^{3+} and the 549 nm ($^5D_4$–$^7F_5$) transition of Tb^{3+} in $KLa(MoO_4)_2$:$0.04Tb^{3+}$,$0.12Eu^{3+}$ microspheres, and the emission intensity of Tb^{3+} $^5D_4$–$^7F_5$ transition obviously decreases compared with that of Tb^{3+} $^5D_4$–$^7F_5$ transition in single $0.04Tb^{3+}$-doped $KLa(MoO_4)_2$ samples. Moreover, Fig. 11 shows the excitation spectrum at Eu^{3+} transition ($^5D_0$–$^7F_2$), we could observe the Tb^{3+} transitions besides Eu^{3+} transitions in the $KLa(MoO_4)_2$:$0.04Tb^{3+}$, $0.04Eu^{3+}$ microcrystals. All of the spectral results illustrate that Tb^{3+} ions may act as an energy donor in the $KLa(MoO_4)_2$ host, in which excitation energy can be transferred to an acceptor Eu^{3+}.

Furthermore, to explore the possibility of the energy transfer, Fig. 12(a) and 12(b) show the variation of PL spectra and emission intensity of $KLa_{(0.96-x)}(MoO_4)_2$:$0.04Tb^{3+}$,xEu^{3+} microcrystals with the increase of Eu^{3+}-doping concentrations from 0 to 0.18, respectively. The sample (x = 0) exhibits typical emissions of Tb^{3+} and is characterized by strong bands at ~549 nm ($^5D_4$→$^7F_5$ transition, green emission) and ~489 nm ($^5D_4$→$^7F_4$ transition, blue emission). Although the concentration of Tb^{3+} was fixed, the emission intensity of Tb^{3+} decreased with increasing Eu^{3+} concentration, indicating that the energy transfer[63,64] from the Tb^{3+} to Eu^{3+} ions is highly efficient since the emission band of the Tb^{3+} ions matches well with the f–f absorptions of the Eu^{3+} ions (Fig. 9). On the contrary, when the Eu^{3+} concentration was fixed with varied Tb^{3+} concentration, the emission intensity of Eu^{3+} dramatically increased with increasing Tb^{3+} concentration in Fig. 12(c) and 12(d). All these results can validate the efficient energy transfer from Tb^{3+} to Eu^{3+}. In addition, it can be seen from Fig. 12(a) and 12(b) that the emission intensity of Eu^{3+} firstly increases with the increase of its

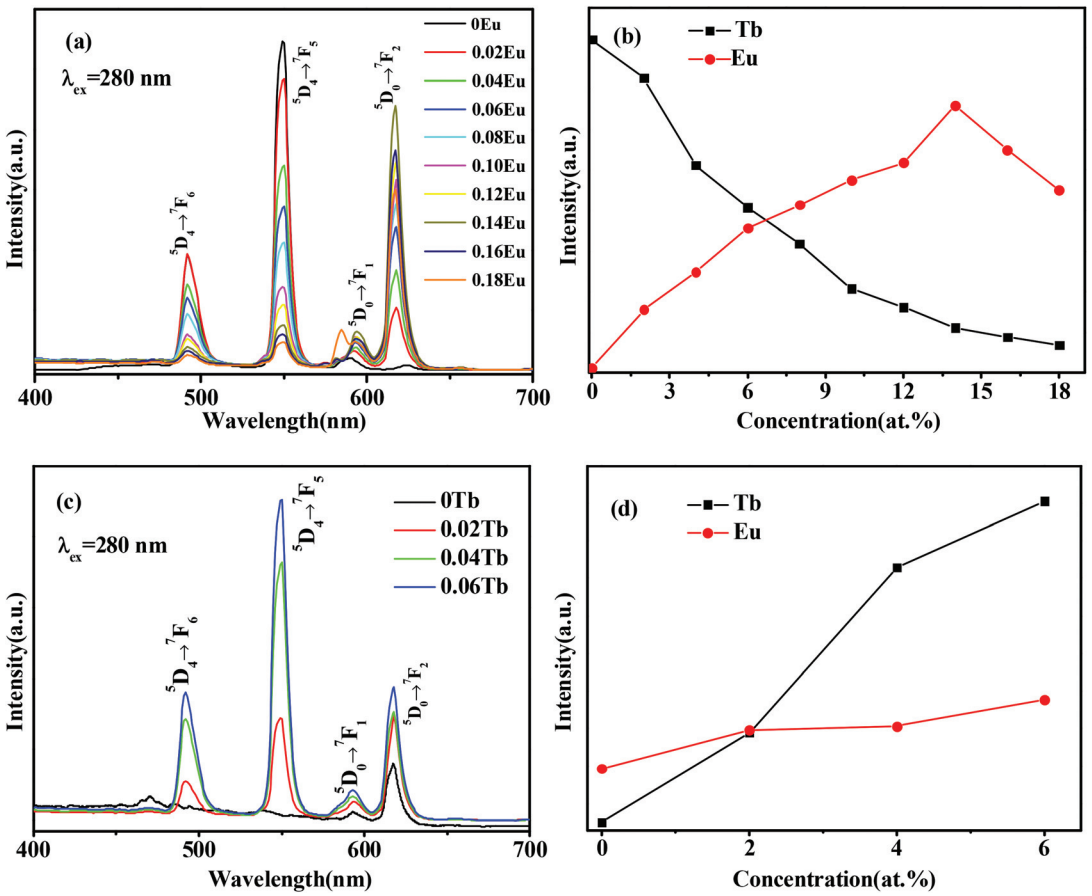

Fig. 12 Emission spectra (a) and relative intensity (b) of the Eu^{3+} and Tb^{3+} emissions of the $KLa_{0.96-x}(MoO_4)_2$:0.04Tb^{3+},xEu^{3+} (x = 0–0.18) microspheres, as a function of the Eu^{3+} content (λ_{ex} = 280 nm). Emission spectra (c) and relative intensity (d) of the 616 nm Eu^{3+} and 549 nm Tb^{3+} emissions of the $KLa_{0.96-y}(MoO_4)_2$:0.04Eu,yTb microspheres (λ_{ex} = 280 nm).

concentration (x), reaching a maximum value at x = 0.14, then decreasing with further increasing (x) due to the concentration quenching effect. When concentration of Eu^{3+} reaches 0.06, we can obtain white light emission because the red (616 nm, Eu^{3+}), green (549 nm, Tb^{3+}) and blue (489 nm, Tb^{3+}) emission bands can be excited efficiently and attain a balance of emission intensity.

Generally, the energy transfer efficiency from a sensitizer to activator can be expressed using the formula:[65–67]

$$\eta_{ET} = 1 - \frac{I_s}{I_{s0}} \quad (1)$$

where η_{ET} is energy transfer efficiency and I_s and I_{s0} are the corresponding intensities of the donor Tb^{3+} emission in the presence and absence of the acceptor Eu^{3+}, respectively. Using eqn (1) the η_{ET} values were obtained as a function of x and are presented in Fig. 13, in which η_{ET} monotonously increases with increasing Eu^{3+} doping concentration and the increscent rate of the emission intensity gradually decreases with the increase of Eu^{3+} concentration. The value is estimated at ~91% for x = 0.18. These high efficiencies of energy transfer primarily originate from the significant spectral overlap between Tb^{3+} emission bands and Eu^{3+} absorption bands, and the energy transfer may occur easily. It depends on the average distance (R) between the Tb^{3+} donor and Eu^{3+} acceptor ions. Exchange interaction generally requires an overlap of the donor and

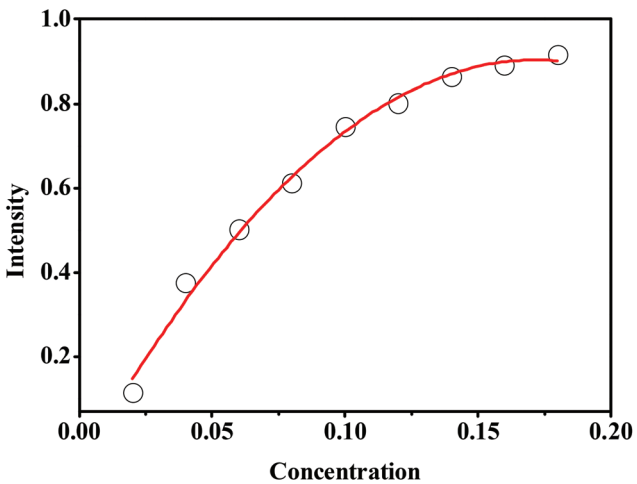

Fig. 13 Energy transfer efficiency (η_{ET}) from Tb^{3+} to Eu^{3+} in $KLa(MoO_4)_2$:0.04Tb^{3+},xEu^{3+} (x = 0–0.18) samples under 280 nm UV excitation.

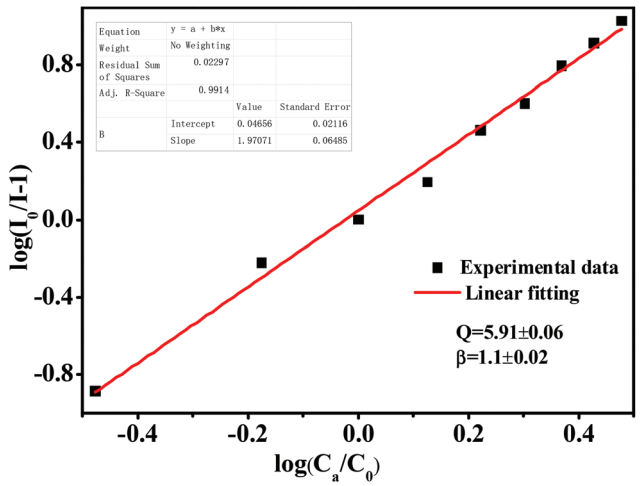

Fig. 14 Plot of intensity variation of Tb^{3+} fluorescence, with Eu^{3+} concentration in relation to Van Uitert's formula.

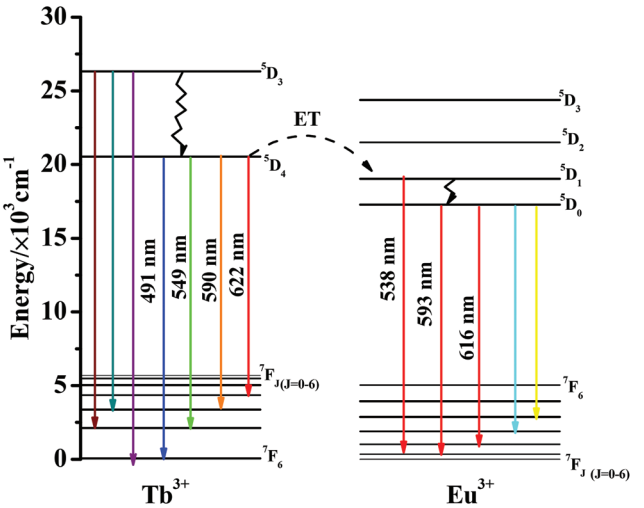

Fig. 15 Energy level scheme representing the energy transfer and energy transfer mechanism in the Tb^{3+}, Eu^{3+}-codoped $KLa(MoO_4)_2$ phosphors.

acceptor orbitals and an R value of less than 0.3–0.4 nm; otherwise, the electric multipole interaction may dominate.[68]

In order to examine the nature of energy transfer, the Van Uitert's formula[69,70] can be expressed by:

$$\log\left(\frac{I_0 - I}{I}\right) = \log\beta + \left(\frac{\theta}{3}\right)\log\left(\frac{C_\alpha}{C_0}\right) \quad (2)$$

where I_0 and I are the intensity of the donor fluorescence in the absence and presence of the acceptor respectively, β is a parameter representing the strength of the multipolar interaction and θ is the separation exponent corresponding to the interaction; C_α is the concentration of the acceptor (Eu^{3+}) and C_0 is the concentration of the acceptor (Eu^{3+}) at which the emission intensity of donor (Tb^{3+}) is quenched to 50% of its original value. θ takes values of 6, 8 or 10 for dipole–dipole, dipole–quadrupole or quadrupole–quadrupole interactions, respectively. We have estimated C_0 to be 5.9 at% and the corresponding plot is shown in Fig. 14, in which the slope ($\theta/3$) is estimated to be 1.97, suggesting that the energy transfer mechanism from the Tb^{3+} to Eu^{3+} ions is a electric dipole–dipole interaction.

Fig. 15 shows energy diagrams of Tb^{3+} and Eu^{3+} and the sensitized Eu^{3+} luminescence mechanism. It can be observed that the energy level of Tb^{3+} ($^5D_4$) is a little higher than that of Eu^{3+} ($^5D_1$ and $^5D_0$), which makes energy transfer through the nonradiative processes possible. In addition, the $^5D_4 \rightarrow {}^7F_{6,5,4,3}$ emission of Tb^{3+} is effectively overlapped with the $^7F_{0,1} \rightarrow {}^5D_{0,1,2}$ absorption of Eu^{3+}, thus the energy transfer from Tb^{3+} to Eu^{3+} is very efficient in general.[71] For the emission of phonons in the $^5D_4$ energy level of Tb^{3+}, part of the energy can transfer to the $^5D_1$ or $^5D_0$ levels of Eu^{3+} by phonon assisted electric dipole–dipole interaction, then relax to $^5D_0$ energy level, and finally transfer to the $^7F_1$ or $^7F_2$ level of Eu^{3+} by radiative transition.

Fig. 16 shows the CIE chromaticity diagram for the emission spectra of the Eu^{3+} and Tb^{3+} co-doped $KLa(MoO_4)_2$ as a

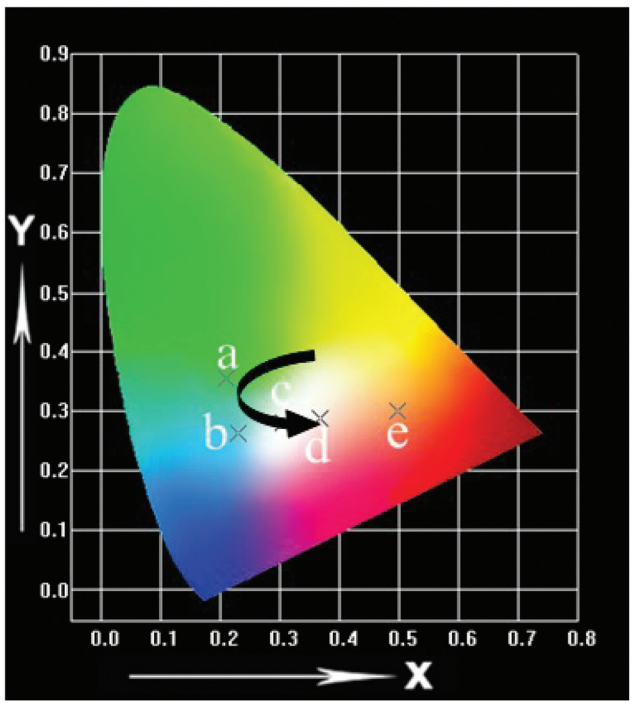

Fig. 16 CIE chromaticity coordinates showing the emission colors for $KLa_{(0.96-x)}(MoO_4)_2$:$0.04Tb^{3+}$,xEu^{3+}, (x = 0, 0.02, 0.06, 0.12, 0.18) phosphors under 380 nm UV excitation: (a) $KLa_{0.96}(MoO_4)_2$:0.04Tb; (b) $KLa_{0.94}(MoO_4)_2$:$0.04Tb^{3+}$,$0.02Eu^{3+}$; (c) $KLa_{0.90}MoO_4)_2$:$0.04Tb^{3+}$, $0.06Eu^{3+}$; (d) $KLa_{0.84}(MoO_4)_2$:$0.04Tb^{3+}$,$0.12Eu^{3+}$; (e) $KLa_{0.78}(MoO_4)_2$: $0.04Tb^{3+}$,$0.18Eu^{3+}$.

function of the Eu^{3+} concentration. It clearly shows that the PL color can be tuned through green, blue, white and red-orange by changing the doping concentration of Eu^{3+} ions due to different energy transfer efficiencies at different Eu^{3+} concentrations. When the concentration of Eu^{3+} varies from 0.06 to

Table 1 CIE color coordinates (*X*, *Y*) of the $KLa_{(0.96-x)}(MoO_4)_2$:0.04Tb^{3+}, *x*Eu^{3+} samples under 380 nm UV excitation

Concentration	CIE chromaticity coordinates	Chromaticity temperature (K)
X = 0.00	(0.211, 0.354)	12 800
X = 0.02	(0.231, 0.263)	23 931
X = 0.06	(0.306, 0.281)	7597
X = 0.12	(0.368, 0.287)	3412
X = 0.18	(0.498, 0.299)	4133

0.12, white light emission can be obtained under 380 nm excitation. The values of CIE parameters for the different concentration doped phosphors are summarized in Table 1. These results indicate that the as-obtained phosphors could the show merits of multicolor emissions in the visible region when excited by a single wavelength light, and might find potential applications in fields such as light display systems and optoelectronic devices.

4. Conclusions

In summary, a series of microsphere $KLa(MoO_4)_2$:Eu^{3+} phosphors with dimension of about 2 μm were prepared by a simple one-step hydrothermal method without using any template, surfactant, or other organic additive. A crystallization pH value of 7 was optimal for the pure-phase synthesis, the emission intensity and the uniform morphology of $KLa(MoO_4)_2$ microcrystals. The formation process of the microspheres was investigated through the homogeneous nucleation, crystallization, aggregation and oriented self-assembling process by time-dependent experiments. The as-synthesized $KLa(MoO_4)_2$:0.15Eu^{3+} microcrystals prepared from the pH = 7 show strongest red emission centered at about 616 nm from Eu^{3+} under UV excitation. By controlling the doping concentration of Eu^{3+}, the luminescence color could be modified through green, blue, white and red-orange easily due to the different composition of emissions of $Tb^{3+}$and Eu^{3+} resulting from different energy efficiencies at different doping concentrations of Eu^{3+}. Moreover, the energy transfer mechanism is proven to be dipole–dipole interaction. These results suggest that the synthesized $KLa(MoO_4)_2$:Eu^{3+},Tb^{3+} spherical structures are promising materials in the white and red regions for the development of color displays.

Acknowledgements

This work was supported by the National Science Foundation of China (no. 11004081), partially sponsored by "Jilin Province Universities Chunmiao Talent" by Department of Education of Jilin Province, and supported by the Science and Technology Development Planning Project of Jilin Province (20130522173JH) and by China Postdoctoral Science Foundation.

References

1 R. J. Xie and N. Hirosaki, *Sci. Technol. Adv. Mater.*, 2007, **8**, 588–600.
2 D. Q. Chen, Y. S. Wang, K. L. Zheng, T. L. Guo, Y. L. Yu and P. Huang, *Appl. Phys. Lett.*, 2007, **91**, 251903.
3 J. W. Wang and P. A. Tanner, *J. Am. Chem. Soc.*, 2010, **132**, 947–949.
4 P. Babu, K. H. Jang, C. S. Rao, L. Shi, C. K. Jayasankar, V. Lavin and H. J. Seo, *Opt. Express*, 2011, **19**, 1836–1841.
5 R. C. Evans, L. D. Carlos, P. Douglas and J. Rocha, *J. Mater. Chem.*, 2008, **18**, 1100–1107.
6 H. S. Peng, M. I. J. Stich, J. B. Yu, L. N. Sun, L. H. Fischer and O. S. Wolfbeis, *Adv. Mater.*, 2010, **22**, 716–719.
7 L. N. Sun, J. B. Yu, H. S. Peng, J. Z. Zhang, L. Y. Shi and O. S. Wolfbeis, *J. Phys. Chem. C*, 2010, **114**, 12642–12648.
8 V. Kumar, A. K. Bedyal, S. S. Pitale, O. M. Ntwaeaborwa and H. C. Swart, *J. Alloys Compd.*, 2013, **554**, 214–220.
9 M. M. Shang, G. G. Li, D. L. Geng, D. M. Yang, X. J. Kang, Y. Zhang, H. Z. Lian and J. Lin, *J. Phys. Chem. C*, 2012, **116**, 10222–10231.
10 P. J. Yadava, C. P. Joshia and S. V. Moharilb, *J. Lumin.*, 2013, **136**, 1–4.
11 D. C. Huang, Y. F. Zhou, W. T. Xu, Z. F. Yang, Z. G. Liu, M. C. Hong, Y. H. Lin and J. C. Yu, *J. Alloys Compd.*, 2013, **554**, 312–318.
12 Z. L. Wang, H. B. Liang, L. Y. Zhou, H. Wu, M. L. Gong and Q. Su, *Chem. Phys. Lett.*, 2005, **412**, 313–316.
13 S. X. Yan, J. H. Zhang, X. Zhang, S. Z. Lu, X. G. Ren, Z. G. Nie and X. J. Wang, *J. Phys. Chem. C*, 2007, **111**, 13256–13260.
14 J. K. Sheu, S. J. Chang, C. H. Kuo, Y. K. Su, L. W. Wu, Y. C. Lin, W. C. Lai, J. M. Tsai, G. C. Chi and R. K. Wu, *IEEE Photonics Technol. Lett.*, 2003, **15**, 18–20.
15 L. N. Sun, Y. N. Qiu, T. Liu, J. Z. Zhang, S. Dang, J. Feng, Z. J. Wang, H. J. Zhang and L. Y. Shi, *ACS Appl. Mater. Interfaces*, 2013, **5**, 9585–9593.
16 S. Neeraj, N. Kijima and A. K. Cheetham, *Chem. Phys. Lett.*, 2004, **387**, 2–6.
17 J. K. Park, C. H. Kim, S. H. Park and H. D. Park, *Appl. Phys. Lett.*, 2004, **84**, 1647–1649.
18 G. A. Kumar, P. R. Biju, G. Jose and N. V. Unnikrishnan, *Mater. Chem. Phys.*, 1999, **60**, 247–255.
19 J. G. Wang, X. P. Jing, C. H. Yan and J. H. Lin, *J. Electrochem. Soc.*, 2005, **152**, G186–G188.
20 S. Ye, C. H. Wang, Z. S. Liu, J. Lu and X. P. Jing, *Appl. Phys. B*, 2008, **91**, 551–557.
21 A. H. Mueller, M. A. Petruska, M. Achermann, D. J. Werder, E. A. Akhadov, D. D. Koleske, M. A. Hoffbauer and V. I. Klimov, *Nano Lett.*, 2005, **5**, 1039–1044.
22 H. S. Yang, D. K. Lee and Y. S. Kim, *Mater. Chem. Phys.*, 2009, **114**, 665–669.
23 K. Y. Jung, J. H. Kim and Y. C. Kang, *J. Lumin.*, 2009, **129**, 615–619.
24 S. Neeraj, N. Kijima and A. K. Cheetham, *Chem. Phys. Lett.*, 2004, **387**, 2–6.

25 F. Wang, Y. Han, C. S. Lim, Y. H. Lu, J. Wang, J. Xu, H. Y. Chen, C. Zhang, M. H. Hong and X. G. Liu, *Nature*, 2010, **463**, 1061–1065.
26 K. Riwotzki, H. Meyssamy, H. Schnablegger, A. Kornowski and M. Haase, *Angew. Chem., Int. Ed.*, 2001, **40**, 573–576.
27 C. Y. Xiang, W. Koo, F. So, H. Sasabe and J. Kido, *Light: Sci. Appl.*, 2013, **2**, e74.
28 E. Matioli, S. Brinkley, K. M. Kelchner, Y. L. Hu, S. Nakamura, S. DenBaars, J. Speck and C. Weisbuch, *Light: Sci. Appl.*, 2012, **1**, e22.
29 G. F. Wang, Q. Peng and Y. D. Li, *J. Am. Chem. Soc.*, 2009, **131**, 14200–14201.
30 P. Li, Q. Peng and Y. D. Li, *Adv. Mater.*, 2009, **21**, 1945–1948.
31 F. Wang and X. G. Liu, *Chem. Soc. Rev.*, 2009, **38**, 976–989.
32 L. N. Sun, W. P. Mai, S. Dang, Y. N. Qiu, W. Deng, L. Y. Shi, W. Yan and H. J. Zhang, *J. Mater. Chem.*, 2012, **22**, 5121–5127.
33 D. Spassky, S. Ivanov, I. Kitaeva, V. Kolobanov, V. Mikhailin, L. Ivleva and I. Voronina, *Phys. Status Solidi C*, 2005, **2**, 65–68.
34 S. S. Kim, S. Ogura, H. Ikuta, Y. Uchimoto and M. Wakihara, *Chem. Lett.*, 2001, **30**, 760–761.
35 R. Sundaram and K. S. Nagaraja, *Sens. Actuators, B*, 2004, **101**, 353–360.
36 B. Yan and J. H. Wu, *Mater. Chem. Phys.*, 2009, **116**, 67–71.
37 L. D. Ivanova, *Zh. Strukt. Khim.*, 1966, **7**, 108.
38 B. M. Wanklyn and F. R. Wondre, *J. Cryst. Growth*, 1978, **43**, 93.
39 E. Cavalli, C. Meschini, A. Toncelli, M. Tonelli and M. Bettinelli, *J. Phys. Chem. Solids*, 1977, **58**, 587–595.
40 J. S. Liao, B. Qiu and H. S. Lai, *J. Lumin.*, 2009, **129**, 668–671.
41 Y. Li, G. F. Wang, K. Pan, Y. Qu, S. Liu and L. Feng, *Dalton Trans.*, 2013, **42**, 3366–3372.
42 N. Banerjee and S. B. Krupanidhi, *Dalton Trans.*, 2010, **39**, 9789–9793.
43 J. Wang, Y. H. Xu and M. Hojamberdiev, *J. Alloys Compd.*, 2009, **481**, 896–902.
44 S. H. Yu, B. Liu, M. S. Mo, J. H. Huang, X. M. Liu and Y. T. Qian, *Adv. Funct. Mater.*, 2003, **13**, 639–647.
45 Q. S. Li, C. H. Feng, Q. Z. Jiao, L. Guo, C. M. Liu and H. B. Xu, *Phys. Status Solidi A*, 2004, **201**, 3055–3059.
46 Y. P. Fang, A. W. Xu, A. M. Qin and R. J. Yu, *Cryst. Growth Des.*, 2005, **5**, 1221–1225.
47 D. Chen, K. B. Tang, F. Q. Li and H. G. Zheng, *Cryst. Growth Des.*, 2006, **6**, 247–252.
48 C. Jia, Y. Cheng, F. Bao, D. Q. Chen and Y. S. Wang, *J. Cryst. Growth*, 2006, **294**, 353–357.
49 H. Wu, H. F. Xu, Q. Su, T. H. Chen and M. M. Wu, *J. Mater. Chem.*, 2003, **13**, 1223–1228.
50 B. Liu, S. H. Yu, L. J. Li, Q. Zhang, F. Zhang and K. Jiang, *Angew. Chem., Int. Ed.*, 2004, **43**, 4745–4750.
51 Y. W. Jun, J. H. Lee, J. S. Choi and J. Cheon, *J. Phys. Chem. B*, 2005, **109**, 14795–14806.
52 X. M. Wang, H. Y. Xu, H. Wang and H. Yan, *J. Cryst. Growth*, 2005, **284**, 254–261.
53 J. G. Li, X. D. Li, X. D. Sun, T. Ikegami and T. Ishigaki, *Chem. Mater.*, 2008, **20**, 2274–2281.
54 J. A. Groenink, C. Hakfoort and G. Blasse, *Phys. Status Solidi A*, 1979, **54**, 329–336.
55 T. Yamase, P. Prokop and Y. Arai, *J. Mol. Struct.*, 2003, **656**, 107–117.
56 C. F. Guo, T. Chen, L. Luan, W. Zhang and D. X. Huang, *J. Phys. Chem. Solids*, 2008, **69**, 1905–1911.
57 Z. L. Fu, H. K. Yang, B. K. Moon, B. C. Choi and J. H. Jeong, *Cryst. Growth Des.*, 2009, **9**, 616–621.
58 B. L. Abrams and P. H. Holloway, *Chem. Rev.*, 2004, **104**, 5783–5801.
59 K. S. Thomas, S. Singh and G. H. Dieke, *J. Chem. Phys.*, 1963, **38**, 2180–2190.
60 H. Guo, F. Li, R. F. Wei, H. Zhang and C. G. Ma, *J. Am. Ceram. Soc.*, 2012, **95**, 1178–1181.
61 X. L. Liang, Z. Y. Lin, Y. X. Yang, Z. W. Xing and G. R. Chen, *J. Am. Ceram. Soc.*, 2012, **95**, 275–279.
62 L. J. Ren, X. H. Lei, X. Q. Du, L. Jin, W. M. Chen and Y. A. Feng, *J. Lumin.*, 2013, **142**, 150–154.
63 S. Mukherjee, V. Sudarsan, R. K. Vatsa, S. V. Godbole, R. M. Kadam, U. M. Bhatta and A. K. Tyagi, *Nanotechnology*, 2008, **19**, 325704.
64 T. K. Anh, L. Q. Minh, N. Vu, T. T. Huong, N. T. Huong, C. Barthou and W. Strek, *J. Lumin.*, 2003, **102–103**, 391–394.
65 G. A. Kumar, P. R. Biju, G. Jose and N. V. Unnikrishnan, *Mater. Chem. Phys.*, 1999, **60**, 247–255.
66 P. I. Paulose, G. Jose, V. Thomas, N. V. Unnikrishnan and M. K. R. Warrier, *J. Phys. Chem. Solids*, 2003, **64**, 841–846.
67 S. Rai and S. Hazarika, *Opt. Mater.*, 2008, **30**, 1343–1348.
68 D. L. Dexter and J. H. Schulman, *Chem. Phys.*, 1954, **22**, 1063–1070.
69 L. G. Van Uitert, *Proc. Int. Conf. Lumin.*, 1966, 1588.
70 L. G. Van Uitert, E. F. Dearborn and J. J. Rubin, *J. Chem. Phys.*, 1966, **45**, 1578–1584.
71 E. Nakazawa and S. Shionoya, *J. Chem. Phys.*, 1967, **47**, 3211–3219.

